Bessel Fourier Orientation Reconstruction: An Analytical EAP Reconstruction Using Multiple Shell Acquisitions in Diffusion MRI

Ameer Pasha Hosseinbor*, Moo K. Chung, Yu-Chien Wu, and Andrew L. Alexander

University of Wisconsin-Madison, Madison, WI, USA
hosseinbor@wisc.edu

Abstract. The estimation of the ensemble average propagator (EAP) directly from **q**-space DWI signals is an open problem in diffusion MRI. Diffusion spectrum imaging (DSI) is one common technique to compute the EAP directly from the diffusion signal, but it is burdened by the large sampling required. Recently, several analytical EAP reconstruction schemes for multiple **q**-shell acquisitions have been proposed. One, in particular, is Diffusion Propagator Imaging (DPI) which is based on the Laplace's equation estimation of diffusion signal for each shell acquisition. Viewed intuitively in terms of the heat equation, the DPI solution is obtained when the heat distribution between temperatuere measurements at each shell is at steady state.

We propose a generalized extension of DPI, Bessel Fourier Orientation Reconstruction (BFOR), whose solution is based on heat equation estimation of the diffusion signal for each shell acquisition. That is, the heat distribution between shell measurements is no longer at steady state. In addition to being analytical, the BFOR solution also includes an intrinsic exponential smootheing term. We illustrate the effectiveness of the proposed method by showing results on both synthetic and real MR datasets.

1 Introduction

The main aim of diffusion-weighted imaging (DWI) is to non-invasively recover information about the diffusion of water molecules in biological tissues, in particular white matter (WM). The EAP contains the full information about the diffusion process, which reflects the complex tissue micro-structure, and its estimation lies at the heart of diffusion MRI. When the narrow pulse condition is met, the EAP is related to the **q**-space diffusion signal E by the Fourier transform:

$$P(\mathbf{p}) = \int E(\mathbf{q}) e^{-2\pi \mathbf{q}\cdot\mathbf{p}} d^3\mathbf{q}, \tag{1}$$

* Corresponding author.

G. Fichtinger, A. Martel, and T. Peters (Eds.): MICCAI 2011, Part II, LNCS 6892, pp. 217–225, 2011.
© Springer-Verlag Berlin Heidelberg 2011

where $\mathbf{p}$ is the displacement vector in propagator-space and $\mathbf{q}$ is the diffusion wave-vector in signal-space. We denote $\mathbf{q} = q\mathbf{u}$ and $\mathbf{p} = p\mathbf{r}$, where $\mathbf{u}$ and $\mathbf{r}$ are 3D unit vectors.

In DTI [2], the diffusion signal is modeled with a Gaussian function. Consequently, DTI can only map a single fiber orientation within a voxel, and fails in voxels with orientational heterogeneity [11]. Diffusion Spectrum Imaging (DSI) [12] is a well known model-free method that uses the Fourier transform to numerically estimate the EAP. It is burdened, however, by the dense sampling required on a Cartesian grid in $\mathbf{q}$-space, which results in long acquisition times.

As a result of the constraints of DSI, several analytical technqiues have arisen that derive an expression for the EAP based on a particular assumption of the diffusion signal. Spherical Polar Fourier Imaging (SPFI) [1, 3] models the signal in terms of an orthonormal basis comprising spherical harmonics (SH) and Gaussian-Laguerre polynomials, and was proposed to sparsely represent $E(\mathbf{q})$. The authors in [10] expanded the diffusion signal in terms of another orthonormal basis that appears in the 3D quantum mechanical harmonic oscillator problem. Their basis is closely related to the SPFI basis. A technique that does not model signal in terms of an orthonormal basis is Diffusion Propagator Imaging (DPI) [7], where the diffusion signal is assumed to be a solution to the 3D Laplace's equation $\bigtriangledown^2 E = 0$. It seems to work well with only a small number samples. However, according to DPI, $E(0)$ does not exist, which makes the assumption of Laplacian equation modeling unrealistic for $E(\mathbf{q})$. Thus, DPI may work well within a range of $\mathbf{q}$ values, but not for the entire $\mathbf{q}$-space.

In this paper, we develop Bessel Fourier Orientation Reconstruction (BFOR), which is a generalized extension of DPI. Rather than assuming the signal satisfies Laplace's equation, we reformulate the problem into a Cauchy problem and assume the signal satisfies the heat equation. The heat equation is a generalization of Laplace's equation, which the latter approaches in the steady state (i.e. $t \to \infty$). It provides an analytical reconstruction of the EAP profile from diffusion signal and models the diffusion signal in terms of an orthonormal basis. In addition, BFOR contains an intrinsic exponential smoothening term that allows one to control the amount of smoothening in the EAP estimation. The last point is significant because, although the Laplacian modeling intrinsically smoothens the diffusion signal, the amount of smoothening can not be controlled, and hence it may oversmooth the signal. We test our method on both synthetic and in vivo datasets.

2 Bessel Fourier Orientation Reconstruction

2.1 Estimation of EAP

Consider the eigenvalue/boundary condition problem

$$\Im_x \psi_i(x) = -\lambda_i \psi_i(x), \quad \psi_i(x = \tau) = 0 \tag{2}$$

which we use to solve the Cauchy problem

$$\frac{\partial}{\partial t}g(x,t) - \Im_x g(x,t) = 0, \quad g(x,0) = f(x), \tag{3}$$

where $f(x)$ is simply the acquired signal and $\Im$ is some self-adjoint linear operator. Chung et al. in [4] derived a unique solution for (3):

$$g(x,t) = \sum_{i=0}^{\infty} a_i e^{-\lambda_i t}\psi_i(x), \tag{4}$$

where $e^{-\lambda_i t}$ is a smoothening term controlled by parameter $t \geq 0$ and the coefficients are given by $a_i = \langle f, \psi_i \rangle$. The implication of (4) is that the solution decreases exponentially as t increases and smoothes out high spatial frequency noise much faster than low-frequency noise. In DPI, however, the steady state assumption permanently removes any temporal term, which governs the extent of smoothening, so there is no smoothening control mechanism. Note that $t = 0$ corresponds to unsmoothened solution.

Within the context of our problem, $g(x,t)$ is **q**-space diffusion signal. The assumption of a 3D Laplacian operator in spherical coordinates allows us to solve (2) via separation of variables, and hence obtain the orthonormal basis $\psi_{nj}(\mathbf{q}) = j_{l(j)}(\frac{\alpha_{nl(j)}q}{\tau})Y_j(\mathbf{u})$,[1] where $\alpha_{nl(j)}$ is n^{th} root of l^{th} order spherical Bessel function of first kind j_l and τ is the radial distance in q-space at which the Bessel function (and hence signal) goes to zero. Y_j are a modified real and symmetric SH basis proposed in [7] to reflect the symmetry and realness of the diffusion signal. The eigenvalues are $\lambda_{nl(j)} = \frac{\alpha^2_{nl(j)}}{\tau^2}$.

The assumption of a Laplacian operator results in (3) becoming the heat equation: $\bigtriangledown^2 E = \frac{\partial E}{\partial t}$. From (4) then, the **q**-space signal can be expanded in terms of the spherical orthonormal basis ψ_{nlm}:

$$E(\mathbf{q},t) = \sum_{n=1}^{N}\sum_{j=1}^{R} C_{nj} e^{\frac{-\alpha^2_{nl(j)}t}{\tau^2}} j_{l(j)}(\frac{\alpha_{nl(j)}q}{\tau})Y_j(\mathbf{u}), \tag{5}$$

where C_{nj} are the expansion coefficients, $R = \frac{(L+1)(L+2)}{2}$ is the number of terms in the modified SH basis of truncation order L, and N is the truncation order of radial basis. Thus, the total number of coefficients in the expansion is $W = \frac{N(L+1)(L+2)}{2}$. Note that the actual acquired signal from scanner is given at $t = 0$.

To derive the EAP, we express the Fourier kernel in (1) as a plane wave expansion in spherical coordinates

$$e^{-2\pi i \mathbf{q}\cdot\mathbf{p}} = 4\pi \sum_{j=1}^{\infty} (-i)^{l(j)} j_{l(j)}(2\pi qp) Y_j(\mathbf{u}) Y_j(\mathbf{r}) \tag{6}$$

Then substituting (5) and (6) into (1), we obtain

[1] For detailed derivations, visit
http://brainimaging.waisman.wisc.edu/∼ameer/Derivations.pdf

$$P(\mathbf{p},t) = 4\pi \int \sum_{n=1}^{N}\sum_{j=1}^{R} C_{nj} e^{\frac{-\alpha_{nl(j)}^2 t}{\tau^2}} j_{l(j)}(\frac{\alpha_{nl(j)} q}{\tau}) Y_j(\mathbf{u}) \sum_{j'=1}^{\infty} (-i)^{l(j')} j_{l(j')}(2\pi qp) Y_{j'}(\mathbf{u}) Y_{j'}(\mathbf{r})\, d^3\mathbf{q}$$
$$= 4\pi \sum_{n=1}^{N}\sum_{j=1}^{R} (-1)^{l(j)/2} C_{nj} e^{\frac{-\alpha_{nl(j)}^2 t}{\tau^2}} Y_j(\mathbf{r}) I_{nl(j)}(p), \tag{7}$$

where we use the orthonormal property of SH, i.e. $\int Y_j(\mathbf{u}) Y_{j'}(\mathbf{u}) d^2\mathbf{u} = \delta_{jj'}$ and define

$$I_{nl(j)}(p) = \int_0^\infty q^2 j_{l(j)}(\frac{\alpha_{nl(j)} q}{\tau}) j_{l(j)}(2\pi qp) dq \approx \int_0^\tau q^2 j_{l(j)}(\frac{\alpha_{nl(j)} q}{\tau}) j_{l(j)}(2\pi qp) dq \tag{8}$$

After some algebra and exploiting properties of the spherical Bessel function, we can write the EAP, for $p > 0$, as

$$P(\mathbf{p},t) = \sqrt{\frac{2\pi^3\tau}{p}} \sum_{n=1}^{N}\sum_{j=1}^{R} (-1)^{\frac{l(j)}{2}} C_{nj} e^{\frac{-\alpha_{nl(j)}^2 t}{\tau^2}} Y_j(\mathbf{r}) \frac{\sqrt{\alpha_{nl(j)}} J_{l(j)-1/2}(\alpha_{nl(j)}) J_{l(j)+1/2}(2\pi\tau p)}{\left(4\pi^2 p^2 - \frac{\alpha_{nl(j)}^2}{\tau^2}\right)} \tag{9}$$

2.2 Implementation of Methods

The task is to estimate coefficients C_{nj} from the observed signal $E(q, \mathbf{u}, t = 0)$. We achieve this by carrying out a linear least square (LS) fitting with regularization in the radial and angular parts. For the LS estimation, denote signal vector by $E = [E(\mathbf{q}_k, t = 0]_{S\times 1}$, the coefficient vector by $C = [C_{nj}]_{W\times 1}$, and the basis matrix by $M = [j_{l(j)}(\frac{\alpha_{nl(j)} q_k}{\tau}) Y_j(\mathbf{u}_k)]_{S\times W}$, where $k = 1, ..., S$. The angular regularization matrix, denoted by $\tilde{L}$, is the Laplace-Beltrami diagonal matrix with $l^2(l+1)^2$ entries on the diagonal and the radial regularization matrix, denoted by $\tilde{N}$, is a diagonal matrix with entries $n^2(n+1)^2$ along its diagonal. The angular and radial regularization matrices penalize, respectively, high degrees of the angular and radial parts of (5) in the estimation under the assumption that they are likely to capture noise [1]. Then the coefficients are $C = (M^T M + \lambda_l \tilde{L} + \lambda_n \tilde{N})^{-1} M^T E$, where λ_l and λ_n are the regularization terms for angular and radial bases, respectively.

Lastly, once we extract the coefficents, the EAP profile at some radius and some instant of smoothening is computed by interpolating Z points along the

equator of a sphere of the same radius (i.e. the polar angle is $\pi/2$ and the azimuthal angle is varied from 0 to 2π). Denoting the EAP vector at given radius p_o and at a given instant t_o of smoothening by $P = [P(p_o, \mathbf{r}_o, t_o)]_{Z\times 1}$ and the $Z \times W$ EAP basis matrix evaluated at p_o and t_o by F, we have $P = FC = F(M^TM + \lambda_l\tilde{L} + \lambda_n\tilde{N})^{-1}M^TE$. It is important to note that we apply smoothening on the EAP, itself, and not on the diffusion signal.

3 Results on Synthetic and Real Data

Synthetic Data. The monoexponential mixture model is frequently used to generate synthetic data to validate a given EAP reconstruction, such as in [1,3], where the maximum b-value used exceeded 3000 s/mm^2. However, diffusion MR imaging experiments using high b-values ($>$ 2000 s/mm^2) have shown that the diffusion signal decay is no longer monoexponential. Studies in normal human brain, with b-values over an extended range of up to 6000 s/mm^2, have shown that the signal decay is better described with a biexponetial curve [9,5]. Thus, we apply BFOR and DPI to simulations of crossing fiber configurations generated via a biexponential mixture model.

In biexponential mixture, $E(\mathbf{q}) = \sum_{k=1}^{N_b}[f_{kf}e^{-b\mathbf{u}^T\mathbf{D}_{kf}\mathbf{u}} + f_{ks}e^{-b\mathbf{u}^T\mathbf{D}_{ks}\mathbf{u}}]$, assuming no exchange between compartments [5, 13]. We look at two equally weighed fibers and set eigenvalues of each diffusion tensor to be [1.6,0.4,0.4]e-3. Diffusion measurements in the corpus callosum were used to simulate fast and slow Gaussian diffusion functions [8]. A hybrid sampling scheme [13] was used and consisted of one baseling image acquired at b=0 s/mm^2 and 6 shells, with $(Ne, b) = \{(6, 690), (21, 2780), (24, 6250), (24, 1.11e4), (100, 1.74e4)\ (100, 2.5e4)\}$, where Ne denotes number of encoding directions, and $q_{max}/\Delta q$=76/15.2 mm^{-1}. Since EAP reconstruction is sensitive to angular resolution, the number of encoding directions is increased with each shell to increase the angular resolution with the level of diffusion weighting. We then add Rician noise the same way as in [6], with $SNR = 1/\sigma$, which is defined as the ratio of maximum signal intensity $S(0) = 1$ to the standard deviation σ of complex Gaussian noise. At $SNR = 10$, 200 trials were simulated. The BFOR parameters are $\{N = 8, L = 6, \tau = 106.4$ mm^{-1}, $\lambda_l = 10^{-6}, \lambda_n = 10^{-6}\}$ and the DPI parameters $\{L = 6, \lambda = 0\}$.

Fig. 1 shows that the BFOR basis fits the diffusion signal nearly perfectly, while Figs. 2 and 4 demonstrate that BFOR successfully captures the geometry and orientation of the EAP profile. The corresponding DPI estimated EAP profiles, shown in Figs. 3 and 5, are not as accurate as BFOR. Fig. 6 shows the Euclidean squared error, averaged over all noise simulations, at various radii for DPI and BFOR, and indicates both methods have a similar robustness to noise. As the smoothening parameter t is increased, the squared error is gradually reduced.

Real Data. We tested our method using healthy, adult human data, with $q_{max}/\Delta q$=76/15.2 mm^{-1} and TE/TR/matrix=122ms/11700ms/128 $\times$ 128 $\times$ 30. The sampling scheme consisted of two baseline images acquired at $b = 0$ s/mm^2 and 5 shells, with (Ne, b)={(6,375),(21,1500),(24,3375),(24,6000),

(a) b=690 (b) b=2780 (c) b=6250 (d) b=1.11e4 (e) b=1.74e4 (f) b=2.50e4

Fig. 1. The ground truth diffusion signal (green) and BFOR estimated signal (red) when noise was absent are compared using all 6 available shells. Two equally weighted fibers were simulated at $t = 0$ crossing at 60°.

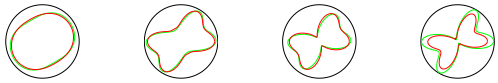

(a) $p = 5$ (b) $p = 15$ (c) $p = 25$ (d) $p = 30$

Fig. 2. The EAP estimated by BFOR (red) and actual EAP (green) in absence of noise for two equally weighed fibers crossing at 60° at $t = 0$ for radii $p = 5$, 15, 25, and 30 μm.

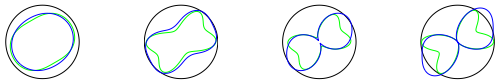

(a) $p = 5$ (b) $p = 15$ (c) $p = 25$ (d) $p = 30$

Fig. 3. The EAP estimated by DPI (blue) and actual EAP (green) in absence of noise for two equally weighed fibers crossing at 60° for radii $p = 5$, 15, 25, and 30 μm

(a) $p = 5$ (b) $p = 15$ (c) $p = 25$ (d) $p = 30$

Fig. 4. The EAP estimated by BFOR (red) and actual EAP (green) in absence of noise for two equally weighed fibers crossing at 90° at $t = 0$ for radii $p = 5$, 15, 25, and 30 μm

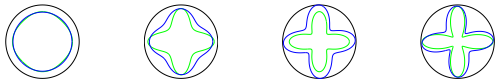

(a) $p = 5$ (b) $p = 15$ (c) $p = 25$ (d) $p = 30$

Fig. 5. The EAP estimated by DPI (blue) and actual EAP (green) in absence of noise for two equally weighed fibers crossing at 90° for radii $p = 5$, 15, 25, and 30 μm

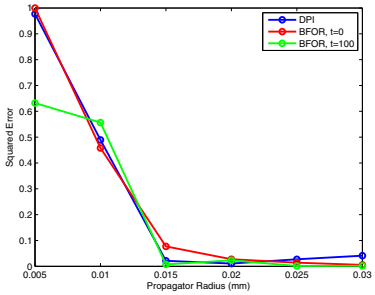

Fig. 6. Plotted is the point-wise mean Euclidean squared error of BFOR and DPI as a function of propagator radius for two fibers crossing at 60° when $SNR = 10$. The squared error is normalized by maximum squared error from BFOR.

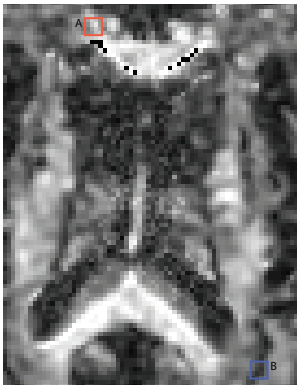

Fig. 7. Axial slice of FA map (b=1500) of adult human brain. `ROI A` on the corpus callosum is a region where we expect single fibers, while `ROI B` is one where we expect crossing fibers (i.e. dark streaks).

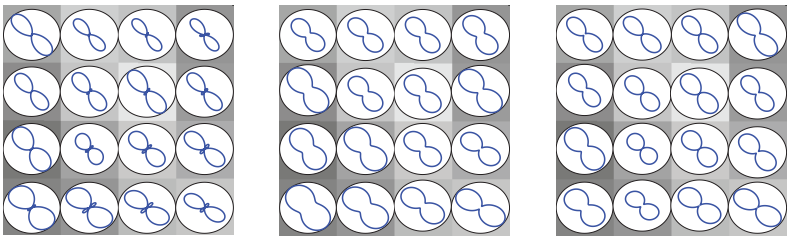

(a) BFOR at $t = 0$ (b) BFOR at $t = 400$ (c) DPI

Fig. 8. Plotted is the EAP profile at $p = 10$ μm overlaid on FA map in `ROI A` using BFOR at (a) $t = 0$, (b) $t = 400$, and (c) DPI

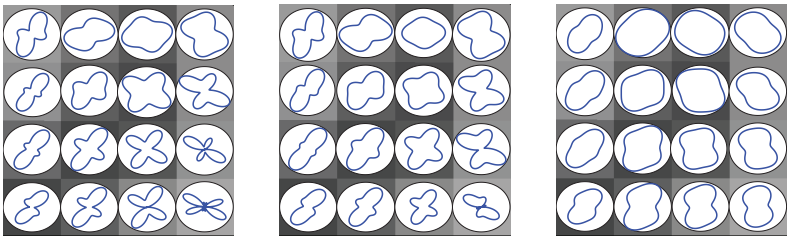

(a) BFOR at $t = 0$ (b) BFOR at $t = 60$ (c) DPI

Fig. 9. Plotted is the EAP profile at $p = 10$ μm overlaid on FA map in `ROI B` using BFOR at (a) $t = 0$, (b) $t = 60$, and (c) DPI. Note how DPI falsely indicates certain WM voxels exhibiting near isotropic diffusion.

(50,9375)} [13]. The number of directions in the outer shells were increased to better characterize complex tissue organization. We set $L = 4$, $N = 4$, $\tau = 91.2$ mm^{-1}, $\lambda_l = 10^{-6}$, $\lambda_n = 10^{-6}$. As shown in Fig. 7, two 4×4 ROIs were drawn on the same slice from a FA map: one on corpus callosum where we expect single fibers, and another on area with black streaks where we expect crossing fibers. The EAP profile was estimated at $p = 10$ μm for each ROI. Based on results shown in Figs. 8 and 9, we see that BFOR performs well in corpus callosum and can successively resolve multiple fiber orientations in voxels with orientational heterogenity. The DPI reconstruction in Fig. 9c, however, erroneously indicates certain WM voxels exhibiting near isotropic diffusion.

4 Discussion

In BFOR, we derive a general solution for the heat equation that is a function of the amount of smoothening t, while DPI solves the heat equation at steady state ($t \to \infty$). This is the first study to include biexponential diffusion model for EAP reconstruction, and the results from the numerical phantom show that BFOR basis models the diffusion signal very well and can successfully reproduce the ground truth EAP. However, the sampling scheme used in the numerical simulations may not be clinically feasible because of the extremely low SNR at b_{max}=2.5e4. The application of BFOR to real data revealed that it can successfully retrieve multiple fiber orientations. Comparison with DPI depicts our model in a favorable light. Future work includes applying compressed sensing to BFOR to find a sparser sampling scheme, and computing quantitative properties of the EAP using BFOR basis.

References

1. Assemlal, H.E., Tschumperlé, D., Brun, L.: Efficient and robust computation of pdf features from diffusion mr signal. Med. Image Anal. 13, 715–729 (2009)
2. Basser, P.J., Mattiello, J., LeBihan, D.: Mr diffusion tensor spectroscopy and imaging. Biophysical Journal 66, 259–267 (1994)
3. Cheng, J., Ghosh, A., Jiang, T., Deriche, R.: Model-free and analytical EAP reconstruction via spherical polar fourier diffusion MRI. In: Jiang, T., Navab, N., Pluim, J.P.W., Viergever, M.A. (eds.) MICCAI 2010. LNCS, vol. 6361, pp. 590–597. Springer, Heidelberg (2010)
4. Chung, M.K., Dalton, K.M., Shen, L., Evans, A.C., Davidson, R.J.: Weighted fourier series representation and its application to quantifying the amount of gray matter. IEEE Transac. Med. Imaging 26, 566–581 (2007)
5. Clark, C.A., Le Bihan, D.: Water diffusion compartmentation and anisotropy at high b values in the human brain. Magn. Reson. Med. 44, 852–859 (2000)
6. Descoteaux, M., Angelino, E., Fitzgibbons, S., Deriche, R.: Regularized, fast, and robust analytical q-ball imaging. Magn. Reson. Med. 58, 497–510 (2007)
7. Descoteaux, M., Deriche, R., LeBihan, D., Mangin, J.F., Poupon, C.: Multiple q-shell diffusion propagator imaging. Med. Image Anal (2010)

8. Maier, S.E., Vajapeyam, S., Mamata, H., Westin, C.F., Jolesz, F.A., Mulkern, R.V.: Biexponential diffusion tensor analysis of human brain diffusion data. Magn. Reson. Med. 51, 321–330 (2004)
9. Mulkern, R.V., Gudbjartsson, H., Westin, C.F., Zengingonul, H.P., Gartner, W., Guttmann, C.R., Robertson, R., Kyriakos, W., Schwartz, R., Holtzman, D., Jolesz, F.A., Maier, S.E.: Multi-component apparent diffusion coefficients in human brain. NMR Biomed. 12, 51–62 (1999)
10. Ozarslan, E., Koay, C., Shepherd, T.M., Blackband, S.J., Basser, P.J.: Simple harmonic oscillator based reconstruction and estimation for three-dimensional q-space mri. In: Proc. Intl. Soc. Mag. Reson. Med. (2009)
11. Tuch, D.S., Reese, T.G., Wiegell, M.R., Makris, N., Belliveau, J.W., Weeden, V.J.: High angular resolution diffusion imaging reveals intravoxel white matter fiber heterogeneity. Magn. Reson. Med. 48, 577–582 (2002)
12. Weeden, V.J., Hagmann, P., Tseng, W.Y.I., Reese, T.G., Weisskoff, R.M.: Mapping complex tissue architecture with diffusion spectrum magnetic resonance imaging. Magn. Reson. Med. 54, 1377–1386 (2005)
13. Wu, Y.C., Alexander, A.L.: Hybrid diffusion imaging. NeuroImage 36, 617–629 (2007)